JOURNAL OF GUIDANCE, CONTROL, AND DYNAMICS
Vol. 25, No. 3, May–June 2002

Guidance and Relative Navigation for Autonomous Rendezvous in a Circular Orbit

Hari B. Hablani,* Myron L. Tapper,† and David J. Dana-Bashian‡
The Boeing Company, Huntington Beach, California 92647

Algorithms for autonomous guidance of spacecraft to approach, to fly around, and to depart from a target vehicle in a circular orbit are presented. The algorithms are based on the closed-form solution of linear Clohessy–Wiltshire equations. The approach and departure algorithms are adaptations of the glideslope guidance used in the past for rendezvous and proximity operations of the space shuttle with other vehicles with astronauts in the guidance loop. The multipulse glideslope algorithms are general, capable of effecting a translation motion of spacecraft in any direction in space autonomously, decelerating while approaching a target or a nearby location, and accelerating while receding. The flyaround algorithm enables the spacecraft to circumnavigate a target spacecraft in any plane, the orbit plane and the local horizontal plane being two special cases thereof. The circumnavigation is performed in a specified period using a specified number of pulses; the larger the number of pulses, the smaller the deviation of flyaround from the specified radius of circumnavigation. The implementation of these algorithms requires estimates of position and velocity of the spacecraft relative to the target. This relative navigation is performed with an extended Kalman filter using range and angle measurements of the target relative to the spacecraft focal plane and the spacecraft attitude estimates from an inertial navigation system. The corresponding measurement models and process noise matrix are provided. Several scenarios are simulated to illustrate the guidance algorithms and relative navigation.

I. Introduction

THIS paper presents simple guidance algorithms to approach, to fly around, and to depart autonomously from a target spacecraft in a circular orbit. Such algorithms have been developed in the context of the space shuttle.[1,2] Pearson[1] emphasized many practical concerns that far outweigh the fuel minimization for rendezvous and presented a pragmatic glideslope algorithm for an in-plane rendezvous using canted thrusters. During the Apollo era, rendezvous of lunar modules with command and service modules were performed,[3] but such rendezvous were especially designed for lunar liftoff and were also assisted by astronauts. Of late, detailed studies, experiments in space, and hardware-in-the-loop laboratory demonstrations of autonomous rendezvous, proximity operation, and docking have proliferated both within the United States[4–7] and overseas.[8–10] Despite these efforts, however, the published literature appears to lack a simple, straightforward, mathematical analysis of guiding a chaser spacecraft to approach, to fly around, and to depart from a target spacecraft. The present paper attempts to fill this need. The guidance algorithms presented here are perhaps simple generalizations and extensions of those in Refs. 1, 2, and 4 and are based on classical linear Clohessy–Wiltshire equations. Consistent with the pragmatism of Ref. 1, the advanced optimal control techniques, such as those in Ref. 11 to minimize fuel consumption using a primer vector, are not called on here.

The paper comprises five sections. Section II summarizes the analytic steps of a classical two-impulse rendezvous. This topic is treated in many textbooks,[12–17] as well as in Ref. 18. Nevertheless, this rendezvous is briefly described here because it is the cornerstone of the so-called glideslope and the flyaround guidance algorithms developed in Secs. III and IV. A glideslope is a straight path from the current location of the chaser spacecraft to its intended destination, which may be a target spacecraft center of mass, a docking port, or a location of interest in space near a target. The history, motivation, and analysis of the glideslope technique in the context of the space shuttle is given in Ref. 1. The glideslope analysis therein is limited to the guidance of the chaser in the orbit plane, using canted thrusters. Pearson[1] formulated a relationship between the glideslope angle, thruster cant angle, range, and range rate. For analysis, the Clohessy–Wiltshire equations in rectilinear coordinates were transformed into polar coordinates. Section III generalizes this algorithm. Here we present, using a matrix formulation instead of the polar formulation of Ref. 1, a general multipulse guidance algorithm to move a chaser vehicle in the vicinity of a target vehicle, decelerating if approaching the target and accelerating if receding away from it. The motion is in any general direction, not limited to tangential direction (V-bar) or radial direction (R-bar), nor restricted to the target orbit plane. Furthermore, it is assumed that, unlike the canted thrusters in Ref. 1, six independent thrusters are available to produce an incremental momentum vector in any direction.

Section IV is concerned with guidance algorithms for flying around a target spacecraft autonomously. A chaser satellite can circumnavigate a target satellite in an in-plane elliptic path in one orbit period, with the target at its center.[19] Under ideal conditions, this elliptic path, once established with proper initial velocity, persists without any additional thruster firing. The largest distance of the chaser from the target is along local horizontal, this distance being twice the shortest distance along local vertical. This elliptic geometry and one complete orbit period for circumnavigation, however, may not always be compatible with the mission requirements. The mission designer may instead require a faster, circular flyaround, perhaps also not necessarily in the orbit plane. As such, Sec. IV presents the formulations for three kinds of flyarounds: natural in-plane elliptic, circular in-plane, and circular in any plane.

The algorithms of Secs. III and IV can be implemented only if the target's orbit and relative location of the chaser are known. Furthermore, real rendezvous, proximity operations, and docking, though lately commonplace with the advent of International Space Station, are extraordinarily complex events because they include, among other things, sensing of the target by the sensors onboard the chaser,

Received 13 February 2001; presented as Paper 2001-4393 at the AIAA Guidance, Navigation, and Control Conference, Montreal, QC, Canada, 9–11 August 2001; revision received 6 November 2001; accepted for publication 6 December 2001.

*Technical Fellow, Flight Systems Design and Analysis, Reusable Space Systems, 5301 Bolsa Avenue. Associate Fellow AIAA.
†Senior Staff Scientist, Phantom Works Advanced Vehicle Design, 5301 Bolsa Avenue.
‡Senior Engineer Scientist, Flight Systems Design and Analysis, Reusable Space Systems, 5301 Bolsa Avenue.

inertial navigation of the chaser and the target vehicles, chaser-target relative navigation, Kalman filtering with or without global positioning system (GPS) receivers on the two vehicles, attitude determination of both vehicles, and more. Reference 2 describes these complexities for rendezvous and docking of the space shuttle with Mir with astronauts in the loop. References 4–6, in contrast, detail autonomous rendezvous and docking using GPS/inertial navigation system (INS), visible/infrared, and video guidance sensors. In this paper, we assume that the target is in a circular orbit and its location known exactly, that the initial relative position of the chaser before initiating any rendezvous operation is known within some error sphere, and that the two vehicles are point masses. Under these assumptions, Sec. V is concerned with the estimation of position and velocity of the chaser spacecraft relative to the target using range and angle measurements of the target and extended Kalman filter. Section VI illustrates the glideslope and circumnavigation algorithms of Secs. III and IV, with or without a Kalman filter. Section VII concludes the paper.

II. Classical Two-Impulse Rendezvous

With reference to Fig. 1, suppose there is a target vehicle in a circular orbit of angular velocity ω. Attached to the vehicle center of mass is a right-handed curvilinear coordinate frame x, y, z, with the x axis along the target velocity vector, $\bar{V}$, or orbit circumference; the z axis radially downward along the vector $\bar{R}$ to the Earth's center of mass; and the y axis completing the right-handed frame. These notations and sign conventions follow those in Ref. 19, though, unfortunately, other notations and conventions are also rife in the literature (see Ref. 13, for instance). The local vertical curvilinear (LVC) frame, instead of the rectilinear frame, might be preferred because the orbital arc distance x of the chaser from the target then can be large.[12,14] However, the chaser–target distances in this paper are so small that the difference between the LVC and the local vertical/local horizontal (LVLH) frame is negligible, less than the sensor noise. Hence, the two frames will not be distinguished in the paper. In the LVLH coordinate system, the motion of a chaser spacecraft located at a station (x, y, z), where x, y, and z are much smaller than the target orbit radius, is governed by the following Clohessy–Wiltshire equations.

Tangential forward:

$$\ddot{x} - 2\omega\dot{z} = \alpha_x \tag{1a}$$

Cross track:

$$\ddot{y} + \omega^2 y = \alpha_y \tag{1b}$$

Radial (down):

$$\ddot{z} + 2\omega\dot{x} - 3\omega^2 z = \alpha_z \tag{1c}$$

where α_x, α_y, and α_z are the acceleration components acting on the chaser in the x, y, z frame. These linear equations are derived and their properties investigated in several textbooks[12–17,19] and in Ref. 18. As is well known, the cross-track motion y normal to the orbit plane is not coupled with the in-plane motion along x and z. The closed-form solution of Eq. (1) is readily available from Refs. 12–19. For convenient manipulations, this analytical solution is arranged in a vector-matrix form, and, to do so, the position and velocity vectors of the chaser vehicle are defined thus[14]:

$$\boldsymbol{r} = [x \quad y \quad z]^T \tag{2a}$$

$$\dot{\boldsymbol{r}} = [\dot{x} \quad \dot{y} \quad \dot{z}]^T \tag{2b}$$

The vector $\boldsymbol{r}$ is not to be confused with the radial downward direction $\bar{R}$ mentioned earlier. Let the initial values of these vectors be, respectively, $\boldsymbol{r}_0$ and $\dot{\boldsymbol{r}}_0$. By the use of the Clohessy–Wiltshire equations, the position and velocity vectors at a later time t are given by

$$\boldsymbol{r}(t) = \Phi_{rr}(t)\boldsymbol{r}_0 + \Phi_{r\dot{r}}(t)\dot{\boldsymbol{r}}_0 \tag{3a}$$

$$\dot{\boldsymbol{r}}(t) = \Phi_{\dot{r}r}(t)\boldsymbol{r}_0 + \Phi_{\dot{r}\dot{r}}(t)\dot{\boldsymbol{r}}_0 \tag{3b}$$

where the four 3×3 Φ matrices are given by[15]

$$\Phi_{rr}(t) = \begin{bmatrix} 1 & 0 & 6(\omega t - s) \\ 0 & c & 0 \\ 0 & 0 & 4 - 3c \end{bmatrix}$$

$$\Phi_{r\dot{r}}(t) = \begin{bmatrix} (4/\omega)s - 3t & 0 & (2/\omega)(1-c) \\ 0 & s/\omega & 0 \\ -(2/\omega)(1-c) & 0 & s/\omega \end{bmatrix}$$

$$\Phi_{\dot{r}r}(t) = \begin{bmatrix} 0 & 0 & 6\omega(1-c) \\ 0 & -\omega s & 0 \\ 0 & 0 & 3\omega s \end{bmatrix}$$

$$\Phi_{\dot{r}\dot{r}}(t) = \begin{bmatrix} -3 + 4c & 0 & 2s \\ 0 & c & 0 \\ -2s & 0 & c \end{bmatrix} \tag{4}$$

and $s = \sin\omega t$, $c = \cos\omega t$. The velocity $\dot{\boldsymbol{r}}_0^+$ required at $\boldsymbol{r}(0)$ at time $t = 0$ to arrive at a specific location, $\boldsymbol{r}_1$, in time T, is obtained easily from Eq. (3a) (Ref. 15):

$$\dot{\boldsymbol{r}}_0^+ = \Phi_{r\dot{r}}^{-1}(\boldsymbol{r}_1 - \Phi_{rr}\boldsymbol{r}_0) \tag{5}$$

The initial velocity at $\boldsymbol{r}_0$, denoted as $\dot{\boldsymbol{r}}_0^- \triangleq \dot{\boldsymbol{r}}_0$, is changed instantaneously to $\dot{\boldsymbol{r}}_0^+$, as depicted in Fig. 2, by imparting an incremental velocity equal to[13]

$$\Delta\boldsymbol{V}_0 = \dot{\boldsymbol{r}}_0^+ - \dot{\boldsymbol{r}}_0^- \tag{6}$$

The arrival velocity at $\boldsymbol{r}_1(T)$, denoted $\dot{\boldsymbol{r}}_1(T)$, is then furnished by Eq. (3b):

$$\dot{\boldsymbol{r}}_1(T) = \Phi_{\dot{r}r}(T)\boldsymbol{r}_0 + \Phi_{\dot{r}\dot{r}}\dot{\boldsymbol{r}}_0^+ \tag{7}$$

If $\boldsymbol{r}_1(T) = 0$, that is, if the chaser is commanded to arrive at the target station at $t = T$, the arrival velocity $\dot{\boldsymbol{r}}_1(T)$ must be annihilated by imparting a pulse $\Delta\boldsymbol{V}_1$ equal to

$$\Delta\boldsymbol{V}_1 = -\dot{\boldsymbol{r}}_1(T) \tag{8}$$

so that, to effect docking, the net relative velocity at $\boldsymbol{r}_1(T)$ is zero.

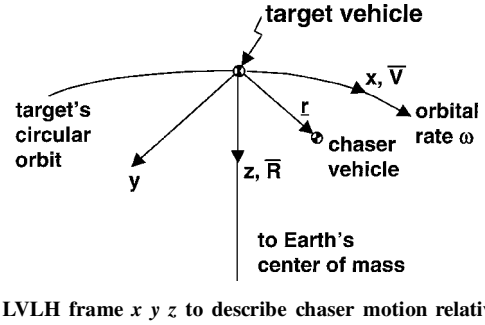

Fig. 1 LVLH frame x y z to describe chaser motion relative to the target.

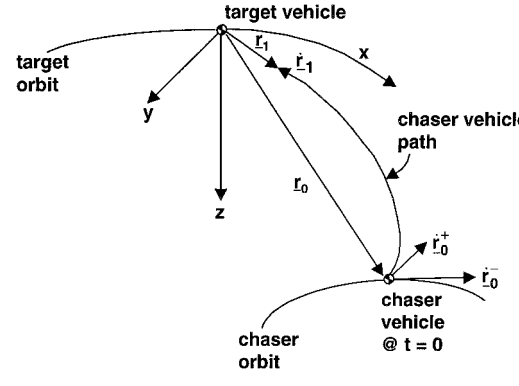

Fig. 2 Two-impulse transfer of chaser vehicle from r_0 to r_1.

The two-impulse scheme just described is highly idealized and unfit for a real rendezvous, but it is useful for formulating the transfer of a chaser vehicle in space near a target circular orbit. Indeed, this scheme enables us to develop the glideslope and circumnavigation guidance algorithms in Secs. III and IV.

III. General Multipulse Glideslope Transfer

Common directions of approaching a target or retracting from it are along the orbital motion in front of the target or from behind, popularly known as the $\bar{V}$ approach, and radial, from below or above the target, known as the $\bar{R}$ approach. However, this relative motion could be in any general direction, either in or out of the orbit plane, including normal to the orbit plane. See Pearson[1] for the examples of in-plane glideslopes. Furthermore, the travel does not have to be directly to the center of mass of the target; instead, the travel may be to some other location of interest. Klumpp[20] considers trajectory shaping by a sequence of velocity increments, but necessary mathematical details are not provided in the paper.

When a chaser vehicle is required to approach a target vehicle, an inbound glideslope guidance is invoked. Likewise, for receding away from the target, an outbound glideslope is called for. In both scenarios, thruster activity near the target is to be minimized to avoid plume impingement on the target vehicle and contamination of its surfaces.[1] In addition, as a chaser approaches the target, its relative velocity must diminish to certain safe limits. These requirements are fulfilled by designing a guidance trajectory wherein the range rate is proportional to the range.[1] In Ref. 1 it is shown that, in a glideslope with continuous thrusting, this relationship, although linear for the most part, is nonlinear near the end. In this paper, for ease of analysis, a linear relationship between the range and range rate is postulated to be the mission design goal, whether the motion is in-plane or out-of-plane. Such guidance trajectories are formulated next for both inbound and outbound glideslopes.

A. Inbound Decelerating Glideslope

Figure 3 illustrates a target in a circular orbit and the associated LVC x, y, z frame at its center of mass. Relative to this frame, at $t=0$, the chaser satellite is located at $\boldsymbol{r}_0$, with its relative velocity equal to $\dot{\boldsymbol{r}}_0^-$. The chaser vehicle is required to arrive at $\boldsymbol{r}=\boldsymbol{r}_T$ in a transfer time T with a velocity specified hereafter. A straight line from $\boldsymbol{r}_0$ to $\boldsymbol{r}_T$, denoted the vector $\boldsymbol{\rho}$ in Fig. 3, is the most natural commanded path for this transfer. Let $\boldsymbol{r}_c(t)$, measured from the target center of mass, be the commanded location of the chaser on this path at time t, $0\le t\le T$. Then the boundary values of $\boldsymbol{r}_c$ are $\boldsymbol{r}_c(0)=\boldsymbol{r}_0$, $\boldsymbol{r}_c(T)=\boldsymbol{r}_T$. The vector $\boldsymbol{\rho}(t)$ emanates from the tip of the vector $\boldsymbol{r}_T$ (Fig. 3), and it defines the commanded location of the chaser on the straight path from $\boldsymbol{r}_0$ to $\boldsymbol{r}_T$. The boundary conditions of $\boldsymbol{\rho}(t)$ are $\boldsymbol{\rho}(0)=\boldsymbol{r}_0-\boldsymbol{r}_T\triangleq\boldsymbol{\rho}_0$, $\boldsymbol{\rho}(T)=0$, and, at any time t, $\boldsymbol{\rho}(t)=\boldsymbol{r}_c(t)-\boldsymbol{r}_T$. Because $\boldsymbol{r}_0\triangleq[x_0\ \ y_0\ \ z_0]^T$ and $\boldsymbol{r}_T\triangleq[x_T\ \ y_T\ \ z_T]^T$, the direction cosines of the vector $\boldsymbol{\rho}$ are given by

$$\cos\alpha=(x_0-x_T)/\rho_0,\qquad \cos\beta=(y_0-y_T)/\rho_0$$
$$\cos\gamma=(z_0-z_T)/\rho_0 \tag{9}$$

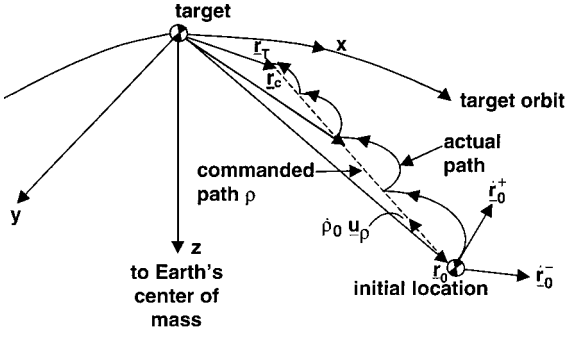

Fig. 3 Three-axis multipulse decelerating inbound glideslope.

where $\rho_0=|\boldsymbol{\rho}_0|$. The direction of the straight path is then given by the unit vector $\boldsymbol{u}_\rho$

$$\boldsymbol{u}_\rho=[\cos\alpha\quad\cos\beta\quad\cos\gamma]^T \tag{10}$$

and the scalar distance ρ, the distance to go, along the vector $\boldsymbol{\rho}$, is $\boldsymbol{\rho}=\rho\boldsymbol{u}_\rho$. The glideslope guidance specifies the distance to go, ρ, as a function of time $\rho(t)$, so that the chaser is commanded to reach $\boldsymbol{r}_T$ from $\boldsymbol{r}_0$ in a period T with the arrival commanded velocity $\dot{\rho}_T\boldsymbol{u}_\rho$ where $\dot{\rho}_T$, less than zero, is some predetermined safe relative speed of the chaser at the distance $|r_T|$ from the target.

As the distance to go, ρ, diminishes, the speed $\dot{\rho}$ must diminish with it. Here, $\dot{\rho}$ is obtained by differentiating ρ, treating the LVLH frame as an inertial nonrotating frame. The following linear relationship between ρ and $\dot{\rho}$ is postulated:

$$\dot{\rho}=a\rho+\dot{\rho}_T \tag{11}$$

where the parameter a (per second), yet to be determined, is the slope of $\dot{\rho}$ vs ρ. The boundary conditions of ρ and $\dot{\rho}$ are, at $t=0$,

$$\rho=\rho_0,\qquad \dot{\rho}=\dot{\rho}_0<0 \tag{12a}$$

and at $t=T$,

$$\rho=0,\qquad \dot{\rho}=\dot{\rho}_T<0 \tag{12b}$$

The initial distance to go, ρ_0, the initial commanded velocity $\dot{\rho}_0<0$, and the final commanded arrival velocity $\dot{\rho}_T<0(|\dot{\rho}_0|>|\dot{\rho}_T|)$, are all known or specified. The slope a is then equal to

$$a=(\dot{\rho}_0-\dot{\rho}_T)/\rho_0<0 \tag{13}$$

The commanded path, Eq. (11), corresponds to a varying commanded acceleration $\ddot{\rho}=a\dot{\rho}$, and because $|\dot{\rho}|$ is decreasing with time, the acceleration (actually deceleration) also decreases with time. These features of the glideslope scheme are desirable. With the boundary conditions (12), the solution to Eq. (11) is

$$\rho(t)=\rho_0\,e^{at}+(\dot{\rho}_T/a)(e^{at}-1) \tag{14a}$$

and the transfer time T is

$$T=(1/a)\,\ln(\dot{\rho}_T/\dot{\rho}_0) \tag{14b}$$

where $a<0$ and $\dot{\rho}_0<\dot{\rho}_T<0$. The algorithm to move the chaser from $\boldsymbol{r}_0$ to $\boldsymbol{r}_T$ can be developed now as follows.

Let the number of thruster firings to travel from $\boldsymbol{r}_0$ ($\rho=\rho_0$) to $\boldsymbol{r}_T$ ($\rho=0$) in time T be N and the uniform interval between any two successive pulses be $\Delta t=T/N$. The thrusters are, thus, fired at time $t_m=m\Delta t\,(m=0,1,\ldots,N-1)$, and the mth pulse pushes the chaser from $\boldsymbol{r}_m(\rho=\rho_m)$ to $\boldsymbol{r}_{m+1}$ ($\rho=\rho_{m+1}$), where

$$\boldsymbol{r}_m=\boldsymbol{r}_T+\rho_m\boldsymbol{u}_\rho \tag{15a}$$

$$\rho_m=\rho(t_m)=\rho_0e^{at_m}+(\dot{\rho}_T/a)(e^{at_m}-1) \tag{15b}$$

The arrival velocity at mth location is $\dot{\boldsymbol{r}}_m^-$, and, in accordance with Eq. (5), the departure velocity $\dot{\boldsymbol{r}}_m^+$ to travel from $\boldsymbol{r}_m$ to $\boldsymbol{r}_{m+1}$ is

$$\dot{\boldsymbol{r}}_m^+=\Phi_{r\dot{r}}^{-1}(\boldsymbol{r}_{m+1}-\Phi_{rr}\boldsymbol{r}_m) \tag{16}$$

where $\Phi_{rr}=\Phi_{rr}(\Delta t)$ and $\Phi_{r\dot{r}}=\Phi_{r\dot{r}}(\Delta t)$. The incremental velocity at $\boldsymbol{r}_m$ is then $\Delta\boldsymbol{V}_m=\dot{\boldsymbol{r}}_m^+-\dot{\boldsymbol{r}}_m^-$, and the chaser will arrive at $\boldsymbol{r}_{m+1}$ with velocity $\dot{\boldsymbol{r}}_{m+1}^-$ equal to

$$\dot{\boldsymbol{r}}_{m+1}^-=\Phi_{\dot{r}r}(\Delta t)\boldsymbol{r}_m+\Phi_{\dot{r}\dot{r}}(\Delta t)\dot{\boldsymbol{r}}_m^+ \tag{17}$$

according to Eq. (7). The actual path of the chaser will not be along the vector $\boldsymbol{\rho}$, of course, but rather will result from the differential spherical gravitational force in Clohessy–Wiltshire equations, the path illustrated in Fig. 3 with humps. Specifically, following Eq. (3a), the path is given by

$$r(t)=\Phi_{rr}(t-t_m)\boldsymbol{r}_m+\Phi_{r\dot{r}}(t-t_m)\dot{\boldsymbol{r}}_m^+ \tag{18}$$

Because the interval between any two successive pulses is the same, the spacecraft will move progressively slower as it approaches the target.

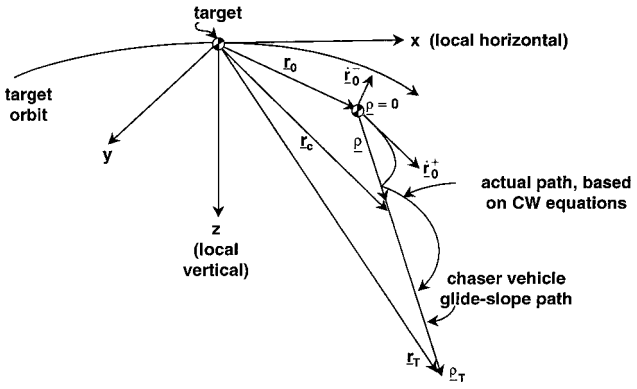

Fig. 4 Three-axis multipulse accelerating outbound glideslope.

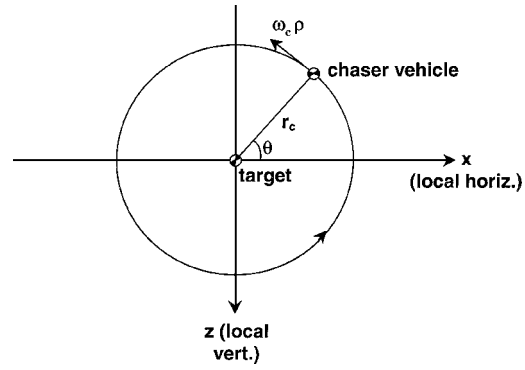

Fig. 5 In-plane circular circumnavigation.

B. Outbound Accelerating Glideslope

The geometry of this glideslope is shown in Fig. 4. Compare this geometry with the geometry of inbound glideslope shown in Fig. 3. The chaser initial radial vector $\boldsymbol{r}_0$ is now closer to the target than the destination radial vector $\boldsymbol{r}_T = \boldsymbol{r}(T)$. The magnitude of the velocity $\dot{\boldsymbol{r}}_0^-$ at $\boldsymbol{r}_0$ is smaller than the specified speed $\dot{\rho}_T$ at $\boldsymbol{r}_T$. The vector $\boldsymbol{\rho}$ now emanates from the initial vector $\boldsymbol{r}_0$ and ends at $\boldsymbol{r}_T$, and at any time t such that $0 \le t \le T$, the commanded glideslope path $\boldsymbol{\rho}(t)$ is defined as $\boldsymbol{\rho}(t) = \boldsymbol{r}_c(t) - \boldsymbol{r}_0$, where, as before, $\boldsymbol{r}_c(t)$ is the vector from the target center of mass to any point on the glideslope path. The boundary conditions of $\boldsymbol{\rho}$ are now

$$\boldsymbol{\rho}(0) = \boldsymbol{0} \tag{19a}$$

$$\boldsymbol{\rho}(T) = \boldsymbol{r}_T - \boldsymbol{r}_0 = [x_T - x_0 \quad y_T - y_0 \quad z_T - z_0]^T \tag{19b}$$

which yields the direction cosines of $\boldsymbol{\rho}$ equal to

$$\cos\alpha = (x_T - x_0)/\rho_T, \qquad \cos\beta = (y_T - y_0)/\rho_T$$

$$\cos\gamma = (z_T - z_0)/\rho_T \tag{20}$$

To accelerate the vehicle while traveling from $\boldsymbol{r}_0$ to $\boldsymbol{r}_T$, the speed $\dot{\rho}$ is postulated to vary linearly with the scalar distance ρ, thus,

$$\dot{\rho} = a\rho + \dot{\rho}_0 \tag{21}$$

where $\rho(0) = 0$, $\rho(T) = \rho_T$, and $\dot{\rho}(0) = \dot{\rho}_0$. The postulated speed at $\boldsymbol{\rho}(T)$ is $\dot{\rho}_T$, and the transfer time from $\rho = 0$ to ρ_T is T. When Eq. (21) is applied for time $t = T$, the positive slope a is

$$a = (\dot{\rho}_T - \dot{\rho}_0)/\rho_T > 0 \tag{22}$$

Solving Eq. (21), one can show now that the distance ρ varies with time; thus,

$$\rho(t) = (\dot{\rho}_0/a)(e^{at} - 1) \tag{23}$$

The transfer time T is still given by Eq. (14b), though a is now positive and $\dot{\rho}_T > \dot{\rho}_0 > 0$.

The algorithm to transfer the vehicle from $\boldsymbol{r}_0$ to $\boldsymbol{r}_T$ is similar to that for the inbound glideslope. N thruster firings effect the transfer, as before, the mth firing taking place at $\boldsymbol{r}(t_m)$, where

$$\boldsymbol{r}(t_m) = \boldsymbol{r}_0 + \rho(t_m)\boldsymbol{u}_\rho \tag{24}$$

and $\rho(t_m)$ is obtained from Eq. (23) by substituting $t = t_m$. The calculation of incremental velocities for each firing proceeds as in Eqs. (16–18).

IV. Circumnavigation

A. In-Plane Natural Elliptic Flyaround

By the use of the solution Eq. (1.17) in Ref. 19, it can be shown that the initial velocity components that a chaser must have to initiate an elliptic, natural flyaround at any location (x, z) are

$$\dot{x} = 2\omega z \tag{25a}$$

$$\dot{z} = -(\omega/2)x \tag{25b}$$

Under ideal conditions, the chaser then will traverse the elliptic path, counterclockwise about the orbit normal y axis,

$$x(t) = x_0 \cos\omega t + 2z_0 \sin\omega t \tag{26a}$$

$$z(t) = -\tfrac{1}{2}x_0 \sin\omega t + z_0 \cos\omega t \tag{26b}$$

where (x_0, z_0) is the initial location of the chaser at $t = 0$. The velocity components $\dot{x}$ and $\dot{z}$ will vary in accordance with Eq. (25). The maximum x and z components of the elliptic path are $x_{\max} = \pm(x_0^2 + 4z_0^2)^{1/2}$, $z_{\max} = \frac{1}{2}x_{\max}$, which define the size of the flyaround.

B. In-Plane Circular

The geometry and notations for this flyaround are shown in Fig. 5. The chaser circumnavigates at a radius r_c from the target center of mass, and its instantaneous angular location in the flyaround circle is θ, where $\theta = 0$ when the chaser is on the circular orbit in front of the target. Suppose the flyaround period is T and the circumnavigation is effected with N pulses. Then the angle traveled between the two pulses m and $m+1$, $m = 0, 1, \ldots, N-1$, is $\Delta\theta = 2\pi/N$. At $t = 0$, the chaser is at a radius r_c at an angle θ_0. Subsequently, the angle θ varies linearly as $\theta = \theta_0 + 2\pi t/T$, and the commanded location of the chaser in the in-plane flyaround circle is

$$x = r_c \cos\theta = r_c \cos(\theta_0 + 2\pi t/T) \tag{27a}$$

$$z = -r_c \sin\theta = r_c \sin(\theta_0 + 2\pi t/T) \tag{27b}$$

The mth pulse takes place at $\theta_m = \theta_0 + m\Delta\theta$, and the corresponding chaser location is defined by the vector $\boldsymbol{r}_m$ equal to

$$\boldsymbol{r}_m = r_c[\cos\theta_m, 0, -\sin\theta_m]^T \tag{28}$$

The strength of this pulse, causing a discrete increment in velocity at $\boldsymbol{r}_m$, is calculated by specifying that, in time T/N, the chaser arrives at $\boldsymbol{r}_{m+1}$ corresponding to the angle $\theta_{m+1} = \theta_0 + (m+1)\Delta\theta$. Because $\boldsymbol{r}_m$ and $\boldsymbol{r}_{m+1}$ have been defined, it is now straightforward to calculate the departure velocity $\dot{\boldsymbol{r}}_m^+$ at $\boldsymbol{r}_m$ and the arrival velocity $\dot{\boldsymbol{r}}_{m+1}^-$ at $\boldsymbol{r}_{m+1}$ using Eqs. (16) and (17), where the transition submatrices are calculated for $t = T/N$.

C. Circular Flyaround in Any Plane

Because in-plane circumnavigation is common, and because it does not excite the out-of-plane motion, the y axis appears to be a natural reference for orienting the axis of an arbitrary flyaround plane. Two angles, θ_{za} about the z axis and θ_{xa} about the once displaced x axis (x' axis, Fig. 6), define the orientation of the flyaround axis y'' or a unit vector $\boldsymbol{a}$ normal to the arbitrary circumnavigation plane $x''z''$ (Fig. 6). When both angles are zero, the y'' axis aligns with the y axis, and the plane $x''z''$ coalesces with the orbit plane xz, as desired. Table 1 records three pairs of special values of the angles θ_{xa} and θ_{za} that bring the y'' axis in alignment with the LVLH x, y, or z axis. The components of the unit vector $\boldsymbol{a}$ along the general y'' axis, expressed in the LVLH frame, are

$$\boldsymbol{a} = \begin{bmatrix} u_{xa} \\ u_{ya} \\ u_{za} \end{bmatrix} = \begin{bmatrix} -\cos\theta_{xa} \sin\theta_{za} \\ \cos\theta_{xa} \cos\theta_{za} \\ \sin\theta_{xa} \end{bmatrix} \tag{29}$$

Table 1 Three special flyaround axes and the corresponding orientation angles

Flyaround Axis	Plane	θ_{xa}, rad	θ_{za}, rad
x	yz	0	$-\pi/2$
y	xz	0	0
z	xy	$\pi/2$	0

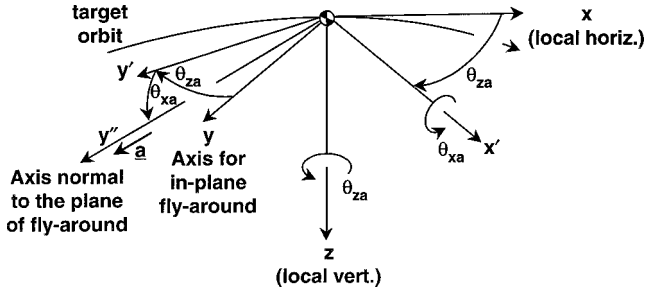

Fig. 6 Orientation of the axis of flyaround in a general plane.

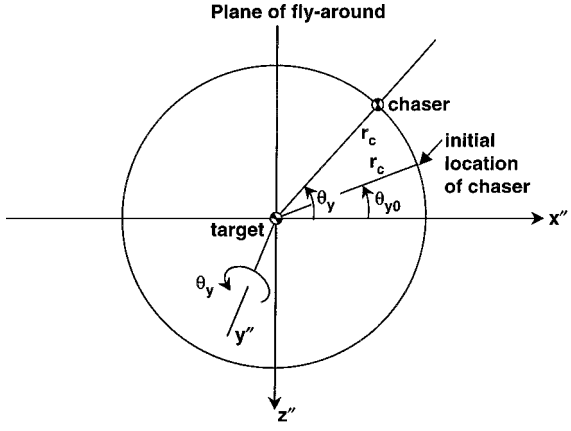

Fig. 7 Location of the chaser vehicle in a general flyaround plane $x''z''$.

If it is easier to specify the unit vector $\boldsymbol{a}$ than to specify the angles, the orientation angles are then determined from

$$\theta_{xa} = \arcsin u_{za} \tag{30a}$$

$$\theta_{za} = \arctan(-u_{xa}, u_{ya}) \tag{30b}$$

where arctan is the four-quadrant arctangent function, often denoted atan2. The commanded location of the chaser in the flyaround plane is defined by the angle θ_y (Fig. 7). At $t = 0$ in Fig. 7, the chaser is located at (x_0, y_0, z_0) corresponding to the angles θ_{za}, $\theta_{xa,}$ and $\theta_y = \theta_{y0}$ in the circumnavigation plane $x''z''$, in this order. To determine θ_{y0}, the initial vector $\boldsymbol{r}_0 = [x_0 \;\; y_0 \;\; z_0]^T$ in the LVLH frame is expressed in the circumnavigation frame $x''y''z''$. One can then show that, in this frame,

$$\boldsymbol{r}_0 = \begin{bmatrix} x_0'' \\ y_0'' \\ z_0'' \end{bmatrix} = \begin{bmatrix} x_0 c\theta_{za} + y_0 s\theta_{za} \\ 0 \\ -s\theta_{xa}(-x_0 s\theta_{za} + y_0 c\theta_{za}) + z_0 c\theta_{xa} \end{bmatrix} \tag{31}$$

where $c_- = \cos_-$, $s_- = \sin_-$. In Eq. (31), because $x''z''$ is the circumnavigation plane of the chaser, the y'' component of the chaser location is zero, by definition. The initial angular location of the chaser, the angle θ_{y0}, is calculated from $\theta_{y0} = \arctan(-z_0'', x_0'')$. At any later time t, the angle θ_y in the $x''z''$ plane equals $\theta_y = \theta_{y0} + 2\pi t/T$ where T is the period specified for a 2π radian circumnavigation. The commanded, instantaneous location of the chaser is now completely specified by the rotation angle θ_y, the orientation angles θ_{za} and θ_{xa}, and the circumnavigation radius r_c. In the LVLH x, y, z frame, this instantaneous location $\boldsymbol{r}$ is given by

$$\boldsymbol{r}(\theta_y(t), \theta_{xa}, \theta_{za}) = r_c \begin{bmatrix} c\theta_{za}c\theta_y - s\theta_{za}s\theta_{xa}s\theta_y \\ s\theta_{za}c\theta_y + c\theta_{za}s\theta_{xa}s\theta_y \\ -c\theta_{xa}s\theta_y \end{bmatrix} \tag{32}$$

The relative location $\boldsymbol{r}$ [Eq. (32)] of the chaser is used for the purpose of effecting a circumnavigation with N pulses. As in the case of in-plane circumnavigation, the mth pulse takes place at $\theta_{y,m} = \theta_{y0} + 2\pi m/N$, $m = 0, 1, \ldots, N-1$. Substituting $\theta_{y,m}$ in Eq. (32), we calculate the vector $\boldsymbol{r}_m$. From then on, this general circumnavigation is commanded similar to the commanding of the in-plane circumnavigation or glideslopes described earlier.

V. Relative Navigation

This section is concerned with the estimation of the position and velocity of the chaser relative to the target. The estimation is accomplished by measuring the range of the target, the location of its image on the focal plane of the chaser, and the attitude of the chaser focal plane in an inertial frame or in the LVLH frame of the chaser. Whereas the focal plane measurements are obtained from cameras and visible or infrared sensors, relative range measurements are provided by lidar, and chaser attitude is furnished by an inertial measurement unit (IMU). Blending all of these measurements suitably, we determine the location of the target relative to the chaser. In the following a simple model of these blended measurements is developed.

A. Measurements Model

Figure 8 depicts the chaser and the target in two neighboring orbits, the target located at $\boldsymbol{r}_{\rm CT}$ from the chaser. Using measurement of the target image centroid on the focal plane and the focal plane attitude measurement from the IMU relative to the chaser LVLH x_1, y_1, z_1 frame, we can express the vector $\boldsymbol{r}_{\rm CT}$ in the triad F_1: x_1, y_1, z_1 as

$$\boldsymbol{r}_{\rm CT}^{F_1} = [r_{{\rm CT}x} \quad r_{{\rm CT}y} \quad r_{{\rm CT}z}]^T \tag{33}$$

Because the lidar, visible, and infrared sensors measure the target location in terms of range and line-of-sight (LOS) angles, Fig. 8 shows two LOS angles, θ_{y1} (azimuth) and θ_{z1} (elevation) measured from the LVLH x_1, y_1, z_1 frame, which bring the local horizontal axis x_1 in alignment with the LOS vector $\boldsymbol{r}_{\rm CT}$. The angle θ_{y1} about the axis y_1 is in the chaser orbit plane and is, thus, called azimuth. The angle θ_{z1} about the once-displaced z_1 axis (that is, z_1' axis) accounts for any out-of-orbit-plane component of the chaser-target vector $\boldsymbol{r}_{\rm CT}$ and is, thus, called elevation. In terms of these angles and the range $r = |\boldsymbol{r}_{\rm CT}|$, the vector $\boldsymbol{r}_{\rm CT}$, Eq. (33), can also be written as

$$\boldsymbol{r}_{\rm CT}^{F_1} = r[c\theta_{y1}c\theta_{z1}, s\theta_{z1}, -s\theta_{y1}c\theta_{z1}]^T \tag{34}$$

For the purposes of rendezvous navigation and guidance using Clohessy–Wiltshire equations, the angles θ_{y1} and θ_{z1} and the range r are the aforementioned blended measurements related to the components $r_{{\rm CT}x}$, $r_{{\rm CT}y}$, and $r_{{\rm CT}z}$ as follows:

$$\begin{aligned} \theta_{y1} &= \arctan(-r_{{\rm CT}z}, r_{{\rm CT}x}) + \nu_y, \qquad \nu_y = \mathfrak{N}(0, \sigma_y) \\ \theta_{z1} &= \arcsin(r_{{\rm CT}y}/r) + \nu_z, \qquad \nu_z = \mathfrak{N}(0, \sigma_z) \\ r &= \left(r_{{\rm CT}x}^2 + r_{{\rm CT}y}^2 + r_{{\rm CT}z}^2\right)^{\frac{1}{2}} + \nu_r, \qquad \nu_r = \mathfrak{N}(0, \sigma_r) \end{aligned} \tag{35}$$

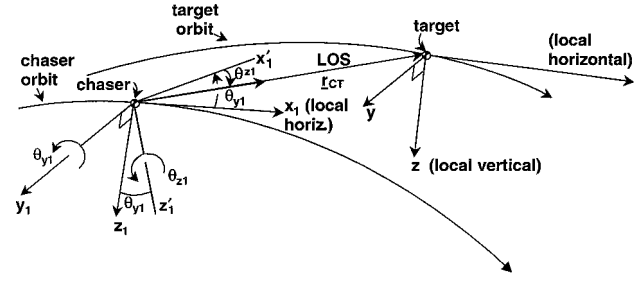

Fig. 8 Target LOS measurement in the chaser LVLH frame.

where ν_y and ν_z are angle measurement noises comprising noise from the visible or infrared sensors and IMU and ν_r is the range measurement noise of lidar. In the absence of any other more suitable model of noise, these noises are assumed to be white, with zero mean and the standard deviations equal to σ_y, σ_z, and σ_r, respectively.

The Clohessy–Wiltshire equations govern the position (x, y, z) of the chaser satellite measured from the target center of mass in the LVLH xyz frame located at the target center of mass. Consequently, the LOS vector $\boldsymbol{r}_{CT}$ and the measurements, Eq. (35), must all be expressed in the target LVLH x, y, z frame. The chaser LVLH x_1, y_1, z_1 frame and the target LVLH x, y, z frame, both shown in Fig. 8, are generally not the same. However, at an altitude of 400 km, when the target and chaser are 1 km or so apart, their orbital angular separation is $\sim$150 μrad, of the same order of magnitude as the visible sensor noise variance ($1\sigma = 120$ μrad) or infrared sensor noise variance ($1\sigma = 850$ μrad–2 mrad). Hence, for such a relatively small separation between a chaser and a target, the two LVLH frames are parallel, and the LOS vector components in the target LVLH frame will be $x = -r_{CTx}$, $y = -r_{CTy}$, and $z = -r_{CTz}$, changing the measurement equations (35) to

$$\begin{aligned}\theta_{y1} &= \arctan(z, -x) + \nu_y = h_1(x, y, z) + \nu_y\\ \theta_{z1} &= \arcsin(-y/r) + \nu_z = h_2(x, y, z) + \nu_z\\ r &= (x^2 + y^2 + z^2)^{\frac{1}{2}} + \nu_r = h_3(x, y, z) + \nu_r\end{aligned} \tag{36}$$

Because these range and angle measurements are related nonlinearly to the position coordinates (x, y, z), the measurement functions h_1, h_2, and h_3 in Eq. (36) are nonlinear. The estimation of position and velocity of the chaser using these measurements and an extended Kalman filter requires partial derivatives of the functions h_1, h_2, and h_3 with respect to the state vector $\boldsymbol{x}$:

$$\boldsymbol{x} = [x \quad y \quad z \quad \dot{x} \quad \dot{y} \quad \dot{z}]^T \tag{37}$$

In particular, rewriting the measurement Eq. (36) in standard Kalman filter vector notations $\boldsymbol{z} = \boldsymbol{h}(x) + \boldsymbol{\nu}$, we require

$$\boldsymbol{H} = \frac{\partial \boldsymbol{h}}{\partial \boldsymbol{x}} = \left[\begin{array}{ccc|c} z/r_{IP}^2 & 0 & -x/r_{IP}^2 & \\ xy/r^2 r_{IP} & -r_{IP}/r^2 & yz/r^2\, r_{IP} & \boldsymbol{0}_{3\times 3} \\ x/r & y/r & z/r & \end{array}\right]_{\hat{r}(-)} \tag{38}$$

where r_{IP} equals in-plane range, $r_{IP}^2 = x^2 + z^2$, $\boldsymbol{H}$ is a 3×6 matrix evaluated at the estimated position $\hat{\boldsymbol{r}}$ just before the measurement update, and $\boldsymbol{0}_{3\times 3}$ is a 3×3 matrix of zeros. The noise vector $\boldsymbol{\nu}$ equals $\boldsymbol{\nu} = [\nu_y \quad \nu_z \quad \nu_r]^T$, and the associated measurement noise matrix $\boldsymbol{R}$ for Kalman gain computations is $\boldsymbol{R} = \text{diag}[\sigma_y^2 \quad \sigma_z^2 \quad \sigma_r^2]$.

B. Process Noise Model

The Clohessy–Wiltshire equations (1) assume that the accelerations α_x, α_y, and α_z are deterministic and known exactly. When thrusters are fired, however, there is likely to be a minute randomness in the force produced. Also, the estimate of the target orbit rate ω is likely to contain a slight random bias error. Because target orbit estimation requires a detailed investigation, possibly along the lines of Refs. 5, 21, and 22, this bias error in the knowledge of ω is ignored here. Let w_x, w_y, and w_z be the white, random acceleration acting on the chaser, in addition to the deterministic acceleration α_x, α_y, and α_z. The intensities of the random accelerations are denoted σ_{wx}, σ_{wy}, and σ_{wz}, respectively, where

$$E\left(w_p^2\right) = \sigma_{wp}^2 \delta(t - \tau), \qquad (p = x, y, z) \tag{39}$$

with δ denoting the Dirac delta operator. The deterministic equations (1) then become as follows.

Tangential, forward (x axis):

$$\ddot{x} - 2\omega\dot{z} = \alpha_x + w_x, \qquad w_x \sim \mathfrak{N}(0, \sigma_{wx}) \tag{40a}$$

Cross track (y axis):

$$\ddot{y} + \omega^2 y = \alpha_y + w_y, \qquad w_y \sim \mathfrak{N}(0, \sigma_{wy}) \tag{40b}$$

Radial, downward (z axis):

$$\ddot{z} + 2\omega\dot{x} - 3\omega^2 z = \alpha_z + w_z, \qquad w_z \sim \mathfrak{N}(0, \sigma_{wz}) \tag{40c}$$

Equations (40) are rewritten in the standard first-order state-space form, with state $\boldsymbol{x}$ defined by Eq. (37). The corresponding 6×6 discrete process noise matrix $\boldsymbol{Q}_k$ can be then shown to be[23,24]

$$\boldsymbol{Q}_k = \left[\begin{array}{ccc|ccc} \sigma_{wx}^2(T^3/3) & 0 & 0 & \sigma_{wx}^2(T^2/2) & 0 & -2\sigma_{wx}^2\omega(T^3/3) \\ & \sigma_{wy}^2(T^3/3) & 0 & 0 & \sigma_{wy}^2(T^2/2) & 0 \\ & & \sigma_{wz}^2(T^3/3) & 2\sigma_{wz}^2\omega(T^3/3) & 0 & \sigma_{\omega z}^2(T^2/2) \\ \hline & & & \sigma_{wx}^2 T + 4\sigma_{wz}^2\omega^2(T^3/3) & 0 & \left(\sigma_{wz}^2 - \sigma_{wx}^2\right)\omega T^2 \\ & & & & \sigma_{wy}^2 T & 0 \\ & & & & & \sigma_{wz}^2 T + 4\sigma_{wx}^2\omega^2(T^3/3) \end{array}\right] \tag{41}$$

where T = sample period. In Eq. (41), the coupling between the in-plane coordinates x and z is retained, though the coupling is weak because at an altitude of 400 km, $\omega \approx 0.001$ rad/s, and for a sample period $T = 1$ s, $\omega T = 0.001$ rad $\ll 1$ rad. For this reason, the coupling terms in $\boldsymbol{Q}_k$, Eq. (41), can be ignored. The process noise matrix associated with each axis agrees with the 2×2 single-axis process noise matrix in Ref. 23.

VI. Illustrations

The preceding guidance algorithms are illustrated now for different scenarios, first with neither noise nor a Kalman filter, and then with noise and a Kalman filter. The target is assumed to be flying at a 400-km altitude ($\omega \approx 0.001$ rad/s, orbit period ≈ 92.56 min).

A. Scenario 1, Inbound/Outbound $\bar{V}$ Glideslope and In-Plane Circumnavigation

Figure 9 illustrates this scenario. Inbound 1 glideslope starts at $x = -500$ m behind the target and ends at $x = -100$ m, effected by 10 pulses in 9 min decelerating the chaser from several meters per second to 0.05 m/s (shown in detail later). Then, after perfect stationkeeping at $x = -100$ m, the chaser performs a 100-m four-pulse circumnavigation in about one orbit period ($\sim$92.53 min). At the end thereof, the inbound 2 glideslope is performed, taking the chaser from $x = -100$ m to -25 m in the next 10 pulses in 9 min. The chaser then perfectly stationkeeps behind the target for 3 min, followed by an outbound accelerating glideslope from -25 to -500 m in 10 pulses over 9 min. One observes in Fig. 9 that the theoretically straight paths, corresponding to the vectors $\boldsymbol{\rho}$ in Figs. 3 and 4 are, in reality, accompanied with humps, diminishing in the case of the decelerating glideslope and growing in the case of the accelerating glideslope. Although the theoretical straight path assumes

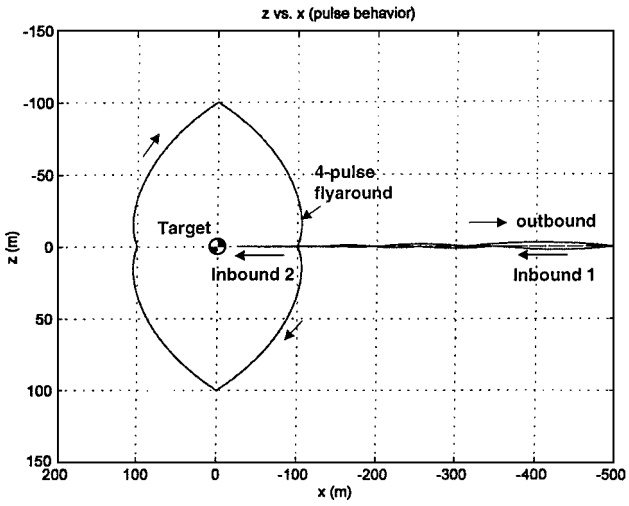

Fig. 9 Inbound, outbound $\bar{V}$ glideslopes and four-pulse in-plane circumnavigation.

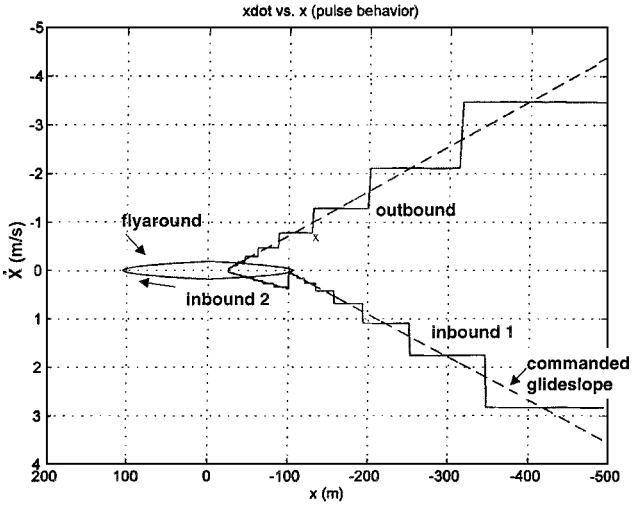

Fig. 10 Phase plane $\dot{x}$ vs x during three $\bar{V}$ glideslopes and a four-pulse 100-m flyaround.

continuous thrusting, the actual glideslope is performed with a finite number of pulses, with coasting between them, and the humps arise during coasting. We also observe that four pulses do not effect a flyaround with a constant radius, the radius being 100 m only at ($\pm$100 m, 0) and (0, $\pm$100 m) in the xz plane. The higher the number of pulses, the better the approximation to a circular flyaround, as illustrated later. The phase plane $\dot{x}$ vs x corresponding to the glideslopes and flyaround in Fig. 9 is shown in Fig. 10. The dashed $\dot{x}$ vs x straight glideslope paths illustrate the $\dot{\rho}$ vs ρ linear variations assumed in the analysis. This continuous increase/decrease in the velocity $\dot{x}$ is realized, on the average, by discrete increments/decrements caused by thruster firings. The circumnavigation over one orbit period is effected with four pulses, taking place at ($\pm$100 m, 0) and (0, $\pm$100 m) in the orbit plane. At $z = \pm 100$ m, ΔV is along $\dot{z}$, as shown in the phase plane $\dot{z}$ vs z, in Fig. 11. The exponential decrement of $\dot{x}$ and its average, discrete counterpart vs time during inbound glideslope over 9 min ($t = 2000$–2540 s), are shown in Fig. 12.

B. Scenario 2, Three-Axis Inbound Glideslope and Flyaround in Local Horizontal Plane

Figure 13 illustrates a three-axis glideslope and a 300-m flyaround in 30 min using equispaced pulses. At $t = 0$, the chaser is located at $[1, 1, 1]^T$ km station, from where it is commanded to arrive at $[300, 0, 0]^T$ m on the x axis using four pulses in 5 min, decelerating the vehicle from 17.56 to 0.084 m/s. The projection of this

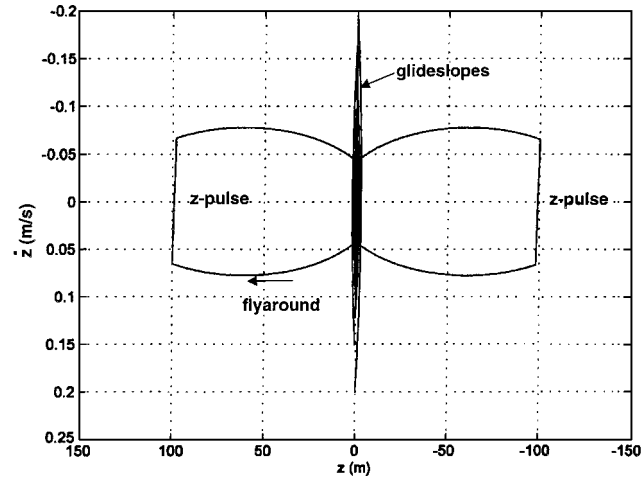

Fig. 11 Phase plane $\dot{z}$ vs z during three $\bar{V}$ glideslopes and a four-pulse 100-m flyaround.

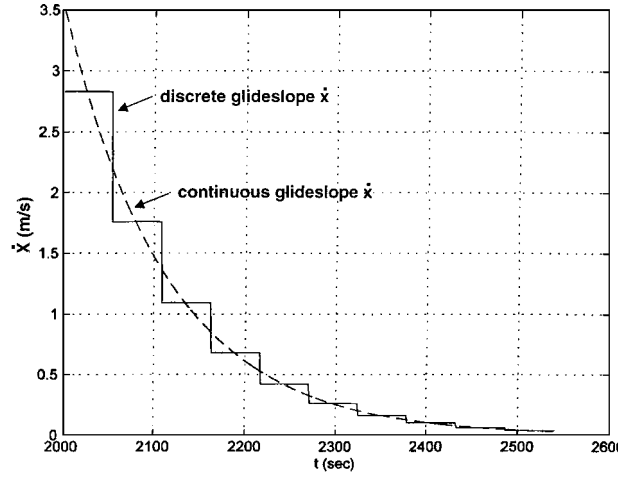

Fig. 12 Exponential discrete deceleration in inbound 1 glideslope.

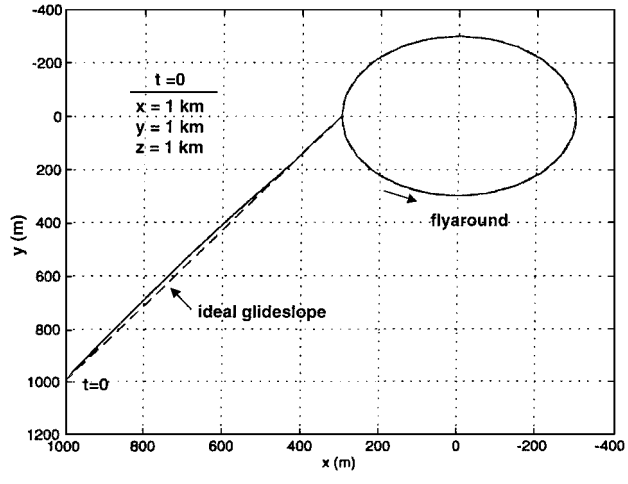

Fig. 13 Three-axis inbound glideslope and 300-m 24-pulse flyaround in (local horizontal) xy plane.

motion in the local horizontal xy plane is shown in Fig. 13. Unlike the 4-pulse in-plane flyaround in Fig. 9, the 24-pulse 30-min flyaround in Fig. 13, following the glideslope, is essentially a circle, commanded here in the xy plane (which is turning about the y axis in an inertial frame at the orbit rate). Because of coupling between x and z, the chaser experiences local vertical motion along z while flying around in the xy plane. This motion, under control by the z component of the pulses, is shown in Fig. 14.

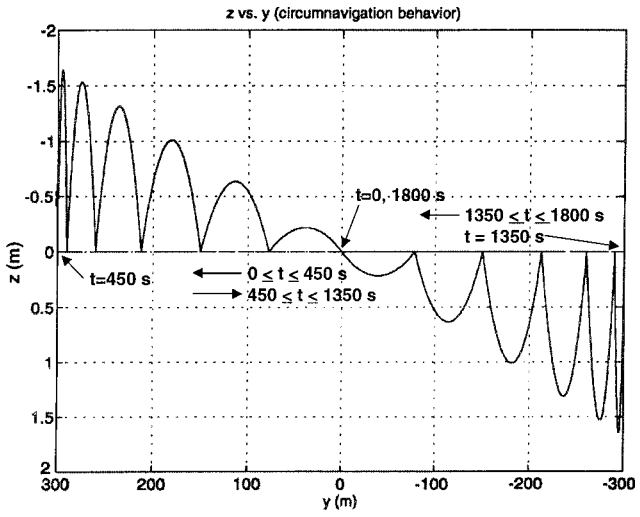

Fig. 14 *Z*-motion induced in a 300-m 24-pulse flyaround in *xy* plane.

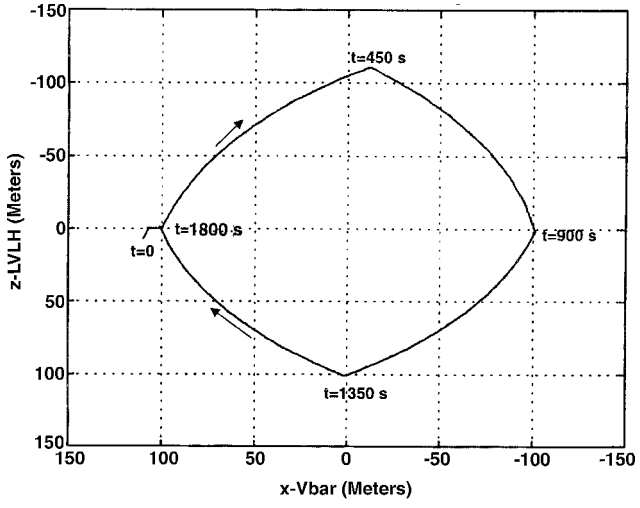

Fig. 15 Four-pulse 30-min in-plane flyaround using range, azimuth, and elevation angle.

C. Scenario 3, Four-Pulse 100-m Flyaround in 30 min Using Sensors and Kalman Filter

Figures 15–18 illustrate this scenario. A total of four sensors, comprising two visible sensors, one infrared sensor, and one lidar sensor, measure the relative location of the target. The visible and infrared sensors provide angle and passive range measurements sequentially at approximately 4 Hz, whereas the lidar sensor provides range measurements at 1 Hz. The measurement noise matrix R for each sensor is

$$\boldsymbol{R}_{\text{visible}} = \text{diag}[(0.001)^2\ \text{rad}^2, (0.001)^2\ \text{rad}^2, (0.08r)^2\ \text{m}^2]$$

$$\boldsymbol{R}_{\text{infrared}} = \boldsymbol{R}_{\text{visible}}, \qquad \boldsymbol{R}_{\text{lidar}} = (0.5\ \text{m})^2 \tag{42}$$

where $r =$ range. The initial estimation error in the state vector $\boldsymbol{x}$ (position in meters, velocity in meters per second) are

$$\tilde{\boldsymbol{x}} = [10\ \text{m}, 0.5\ \text{m}, 7\ \text{m}, -0.02\ \text{m/s}, -0.02\ \text{m/s}, -0.02\ \text{m/s}]^T \tag{43}$$

and the covariance matrix $\boldsymbol{P}$ is initialized as

$$\boldsymbol{P} = \text{diag}[33.3\ \text{m}^2, 33.3\ \text{m}^2, 33.3\ \text{m}^2, 0.0025\ (\text{m/s})^2, 0.0025\ (\text{m/s})^2, 0.0025\ (\text{m/s})^2] \tag{44}$$

The incremental velocity vector $\Delta \boldsymbol{V}$, determined by the guidance algorithm, is produced by thrusters with 1% error and measured by the accelerometer with 2% error. These errors are compensated for by specifying the process noise acceleration variance $\sigma_{wx}^2 T = \sigma_{wz}^2 T = (0.004\ \text{m/s})^2$ and $\sigma_{wy}^2 = 10^{-4} \times \sigma_{wx}^2$ in Eq. (41). The sample period T varies, but is nominally equal to 0.25 s.

The results in Figs. 15–18 pertain to the just-mentioned specifications. The impulses for circumnavigation are calculated using the estimated position, either from the Kalman filter or from knowledge of the initial conditions, not the true position of the chaser. As such, the chaser is not expected to reach its intended place exactly. In Fig. 15, $\Delta \boldsymbol{V}$, calculated at $t = 0$ to move the chaser from (100, 0, 0) m to (0, 0, −100) m in $t = 450$ s using the initial position estimate according to the estimation error (43), takes the vehicle not to its intended place exactly, but in the neighborhood thereof. Aided by the sensors, however, particularly the lidar, the initial estimation errors subside to an optimum level determined by the ratio of the process noise matrix $\boldsymbol{Q}$ and the measurement noise matrix $\boldsymbol{R}$ specified earlier. See in Fig. 15 that at $t = 900$, 1350, and 1800 s, the chaser essentially reaches its intended location. The variation

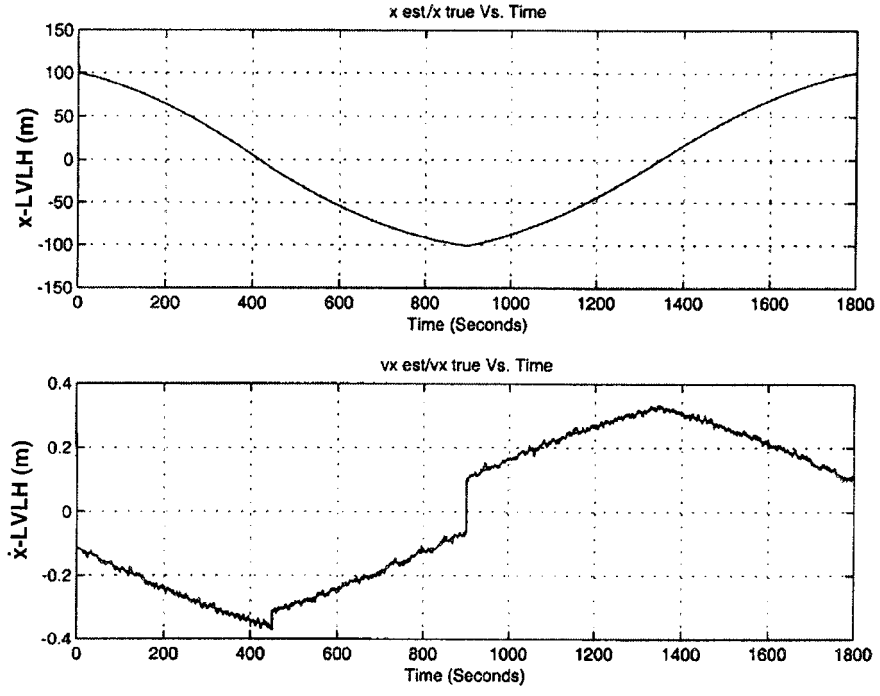

Fig. 16 Position component x, velocity component $\dot{x}$, and their estimates $\hat{x}$ and $\hat{\dot{x}}$ vs flyaround time t.

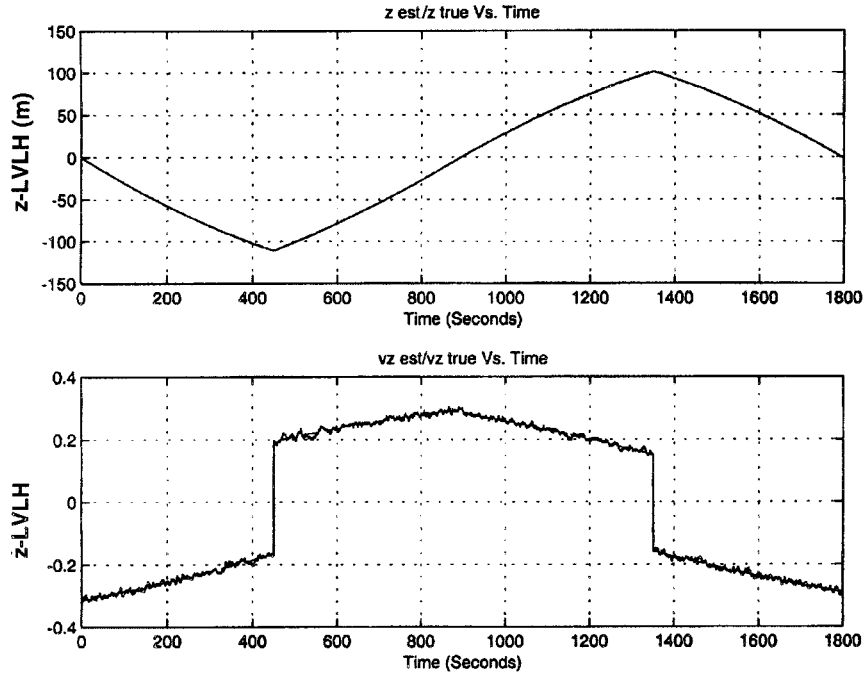

Fig. 17 Position component z, velocity component $\dot{z}$, and their estimates $\hat{z}$ and $\hat{\dot{z}}$ vs flyaround time t.

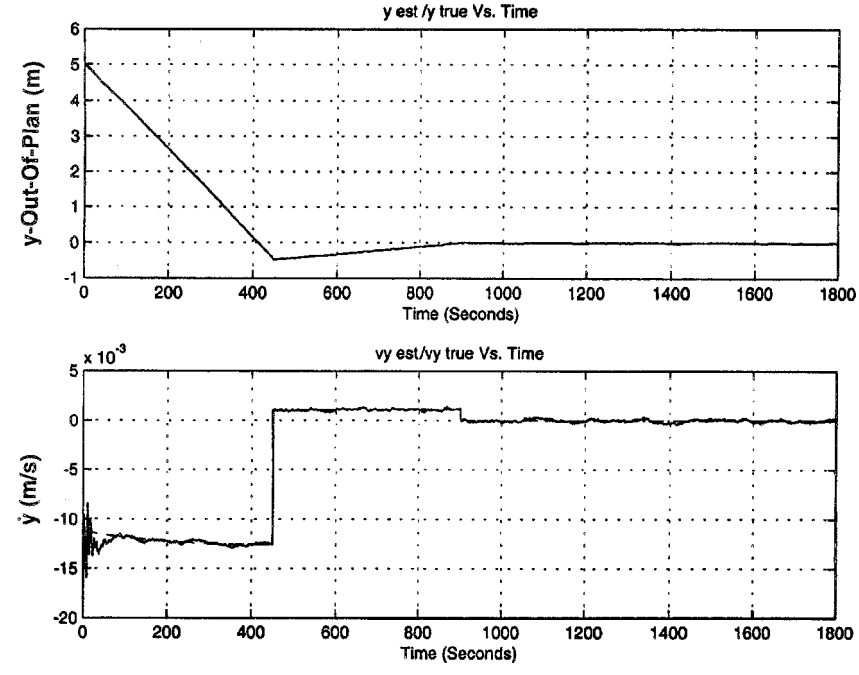

Fig. 18 Position component y, velocity component $\dot{y}$, and their estimates $\hat{y}$ and $\hat{\dot{y}}$ vs flyaround time t.

of the true and the estimated position coordinates x, y, z and $\hat{x}$, $\hat{y}$, $\hat{z}$, respectively, and the velocity components $\dot{x}$, $\dot{y}$, $\dot{z}$, and $\hat{\dot{x}}$, $\hat{\dot{y}}$, $\hat{\dot{z}}$, respectively, vs time is shown in Figs. 16–18. Because of active range measurements with lidar, the initial position estimation errors, Eq. (43), are removed quickly because the true and the estimated position coordinates in Figs. 16–18 do not appear distinguishable. Some estimation errors in velocity estimates persist, however, particularly due to the 2% bias error in the accelerometer measurements of ΔV, as seen in Figs. 16–18. The two significant discrete steps in $\dot{x}$ and its estimate $\hat{\dot{x}}$ at $t = 0$ and 900 s in Fig. 16 change the direction (slope) of x motion near $x = \pm 100$ m, seen in Fig. 15. Likewise, the discrete steps in $\dot{z}$ and $\hat{\dot{z}}$ in Fig. 17 at $t = 450$ and 1350 s change the direction of z motion near $z = \pm 100$ m in Fig. 15. The in-plane (x, z) motion is not coupled with the y motion, but because the chaser is initially 5 m out-of-orbit-plane, it is brought in-plane, and y is decreased to nearly zero in just the first three pulses, at $t = 0$, 450, and 900 s, as depicted in Fig. 18. To conserve space, the position and velocity estimation errors, $\tilde{x}$, $\tilde{y}$, $\tilde{z}$, and $\tilde{\dot{x}}$, $\tilde{\dot{y}}$, $\tilde{\dot{z}}$, respectively, and the positive and negative square roots of their variances, $P(\tilde{x}^2)$, $P(\tilde{y}^2)$, $P(\tilde{z}^2)$ and $P(\tilde{\dot{x}}^2)$, $P(\tilde{\dot{y}}^2)$, $P(\tilde{\dot{z}}^2)$, respectively, are not shown here, though they are displayed in Ref. 25. All variables concerning $\tilde{x}$ and $\tilde{z}$ exhibit a cyclic behavior, reflecting the cyclic variation of x and z in the flyaround, and the estimation errors remain within the bounds of their respective standard deviations.

D. Scenario 4, Inbound/Outbound Glideslopes, Circumnavigation, and Stationkeeping Using Sensors and Kalman Filter

Figures 19 and 20 illustrate a scenario similar to scenario 1, but now using sensors and Kalman filter, as described in scenario 3, and a circumnavigation using 24 pulses. Figure 19 depicts all phases of motion: inbound and outbound glideslopes, flyaround, and stationkeeping. The duration of each phase appears in Fig. 19. Because of active range measurement and relatively small measurement errors, the true and the estimated x and z position components in Fig. 19

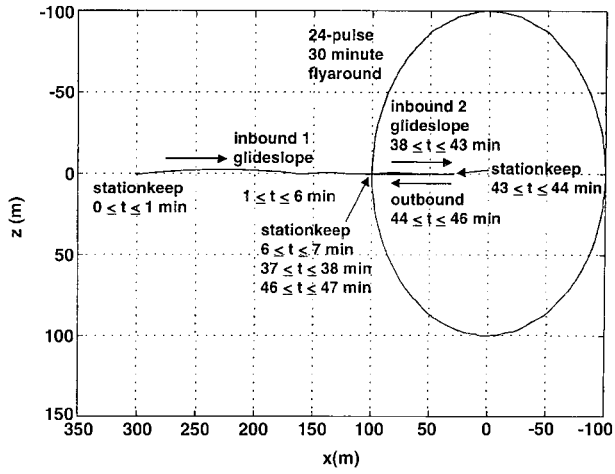

Fig. 19 In-plane inbound/outbound glideslopes, 24-pulse circumnavigation, and stationkeeping using sensors and Kalman filter.

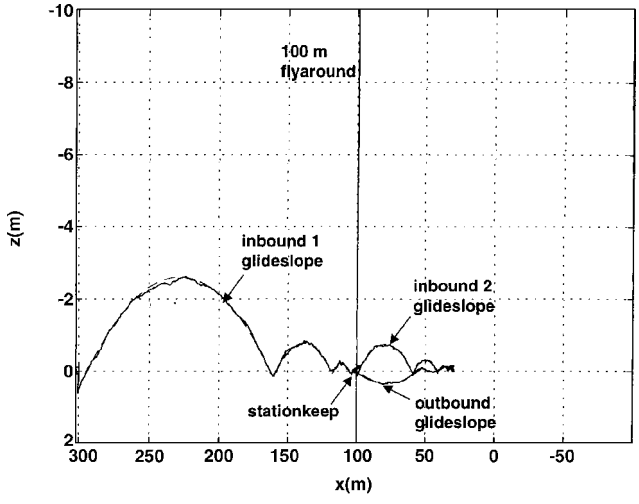

Fig. 20 Glideslopes magnified.

are almost indistinguishable. The three glideslopes are shown at a magnified scale in Fig. 20, where the estimates $\hat{x}$ and $\hat{z}$ are seen to track the true x and z well.

Conclusions

The autonomous guidance algorithms developed and illustrated in the preceding text for glideslope and circumnavigation are simple because they are based on classical Clohessy–Wiltshire equations, their solutions, and elementary vector and matrix analysis of kinematics. Different NASA centers and industries may already have similar or even advanced algorithms based on Lambert guidance, but, apparently, the algorithms are not available in the literature. Notwithstanding the simplicity of the algorithms, however, their implementation entails complex sensor technology for inertial and relative navigation. The relative navigation is briefly treated in the paper, utilizing range, azimuth, and elevation measurements and an extended Kalman filter. However, the initial relative position and velocity estimates, to be used in relative navigation, are extracted from inertial navigation of the chaser and the target, and this complex subject is not considered in the paper. Also, the angle measurements from the visible or infrared sensors may be biased and the sensor focal planes may be misaligned. The designer/analyst must consider, in addition, IMU measurements, attitude dynamics of both chaser and target, their attitude determination, and attitude control of the chaser to fire the thrusters in the right direction. These topics and others will be addressed in the future.

Acknowledgments

The authors are grateful to Thomas A. Mulder and his associates, Rendezvous and Proximity Operations Group, The Boeing Company, Houston, Texas, for sharing their rendezvous techniques used on the space shuttle over nearly two decades. Also, the authors are indebted to J. Brazzel, The Boeing Company, Houston, Texas, and F. Clark and P. Spehar, Lockheed Martin, Houston, Texas, for their briefing material entitled *RPOP Guidance Algorithms*, 24 February 2000. Their work is the cornerstone of the study reported here.

References

[1]Pearson, D. J., "The Glideslope Approach," *Advances in the Astronautical Sciences*, Vol. 69, American Astronautical Society, San Diego, CA, 1989, pp. 109–123; also AAS Paper 89-162.

[2]Zimpfer, D., and Spehar, P., "STS-71 Shuttle/Mir GNC Mission Overview," *Advances in the Astronautical Sciences*, Vol. 93, Pt. I, American Astronautical Society, San Diego, CA, 1996, pp. 441–460; also AAS Paper 96-129.

[3]Young, K. A., "Apollo Lunar Rendezvous," *Journal of Spacecraft and Rockets*, Vol. 7, No. 9, 1970, pp. 1083–1086.

[4]Cruzen, C. A., Lomas, J. J., and Dabney, R. W., "Test Results for the Automated Rendezvous and Capture System," *Advances in the Astronautical Sciences*, Vol. 104, American Astronautical Society, San Diego, CA, 2000, pp. 35–56; also AAS Paper 00-003.

[5]Upadhyay, T., Cotterill, S., and Deaton, A. W., "Autonomous Reconfigurable GPS/INS Navigation and Pointing System for Rendezvous and Docking," AIAA Paper 92-1390, March 1992.

[6]Howard, R. T., Bryan, T. C., Brook, M. L., and Dabney, R. W., "The Video Guidance Sensor: A Flight Proven Technology," *Advances in the Astronautical Sciences*, American Astronautical Society, San Diego, CA, 1999, pp. 281–298; also AAS Paper 99-025.

[7]Calhoun, P., and Dabney, R., "A Solution to the Problem of Determining the Relative 6 DOF State for Spacecraft Automated Rendezvous and Docking," Vol. 2466, Society of Photo-Optical Instrumentation Engineers, Bellingham, WA, 1995, pp. 175–185.

[8]Kawano, I., Mokuno, M., Kasai, T., and Suzuki, T., "Result and Evaluation of Autonomous Rendezvous Docking Experiments of ETS-VII," *Proceedings of the AIAA Guidance, Navigation, and Control Conference*, AIAA, Reston, VA, 1999, pp. 1–9.

[9]Philip, N. K., Ananthasayanam, M. R., and Dasgupta, S., "Study of Relative Position and Attitude Estimation and Control Scheme for the Final Phase of an Autonomous Docking Mission," *IFAC Automatic Control in Aerospace*, Elsevier Science, Kidlingfon, U.K., 1998, pp. 185–193.

[10]Serrano-Martinez, J. B., "Use of Simulation Tools and Facilities for Rendezvous and Docking Missions," Vol. CP-561, *Space Systems Design and Development Testing*, AGARD, Neuilly Sur Seine, France, 1994, pp. 17.1–17.12.

[11]Prussing, J. E., and Chiu, J. H., "Optimal Multi-Impulse Time-Fixed Rendezvous Between Circular Orbits," *Journal of Guidance, Control, and Dynamics*, Vol. 9, No. 1, 1986, pp. 17–22.

[12]Kaplan, M. H., *Modern Spacecraft Dynamics and Control*, Wiley, New York, 1976, Sec. 3.6, pp. 108–115.

[13]Prussing, J. E., and Conway, B. A., *Orbital Mechanics*, Oxford Univ. Press, New York, 1993, Chap. 8.

[14]Chobotov, V. A. (ed.), *Orbital Mechanics*, AIAA Education Series, AIAA, Washington, DC, 1991, Chap. 7.

[15]Wiesel, W. E., *Spaceflight Dynamics*, McGraw–Hill, New York, 1997, Sec. 3.5.

[16]Wie, B., *Space Vehicle Dynamics and Control*, AIAA Education Series, AIAA, Reston, VA, 1998, Sec. 4.6.

[17]Vallado, D. A., *Fundamentals of Astrodynamics and Applications*, McGraw–Hill, New York, 1997, Sec. 5.8.

[18]Mullins, L. D., "Initial Value and Two-Point Boundary Value Solutions to the Clohessy–Wiltshire Equations," *Journal of the Astronautical Sciences*, Vol. 40, No. 4, 1992, pp. 487–501.

[19]Bryson, A. E., Jr., *Control of Spacecraft and Aircraft*, Princeton Univ. Press, Princeton, NJ, 1994, Chap. 1.

[20]Klumpp, A. R., "Trajectory Shaping Rendezvous Guidance," *IEEE Aerospace and Electronics Systems Magazine*, Vol. 2, Pt. 2, 1987, pp. 17–22.

[21]Park, Y. W., Brazzell, J. P., Jr., Carpenter, J. R., Hinkel, H. D., and Newman, J. H., "Flight Test Results from Real-Time Relative Global Positioning System Flight Experiment on STS-69," NASA TM-104824, Nov. 1996.

[22]Garrison, J. L., and Axelrod, P., "Application of the Extended Kalman Filter for Relative Navigation in an Elliptic Orbit," *Advances in the Astronautical Sciences*, American Astronautical Society, San Diego, CA, 1996, pp. 693–711; also AAS Paper 96-142.

[23]Bar-Shalom, Y., and Li, X.-R., *Estimation and Tracking: Principles, Techniques, and Software*, self-published, 1998, pp. 262, 263.

[24]Gelb, A. (ed.), *Applied Optimal Estimation*, MIT Press, Cambridge, MA, 1974, Sec. 3.6.

[25]Hablani, H. B., Tapper, M. A., and Dana-Bashian, D. J., "Guidance Algorithms for Autonomous Rendezvous of Spacecraft with a Target Vehicle in Circular Orbit," *Proceedings of the AIAA Guidance, Navigation, and Control Conference*, AIAA, Reston, VA, 2001, pp. 1–15.